Available online at www.sciencedirect.com
SCIENCE DIRECT®
Scripta Materialia 55 (2006) 35–40
Scripta MATERIALIA
www.actamat-journals.com

Viewpoint Paper

An atom-probe tomographic study of the temporal evolution of the nanostructure of Fe–Cu based high-strength low-carbon steels

Dieter Isheim,[a,b,*] R. Prakash Kolli,[a] Morris E. Fine[a] and David N. Seidman[a,b]

[a] *Department of Materials Science and Engineering, Northwestern University, Evanston, IL 60208-3108, USA*
[b] *Northwestern University Center for Atom-Probe Tomography (NUCAPT), Northwestern University, Evanston, IL 60208-3108, USA*

Received 1 November 2005; revised 7 February 2006; accepted 13 February 2006
Available online 31 March 2006

Abstract—A three-dimensional (3D) knowledge of the atomic-scale structure is necessary for improving the design and understanding of modern materials with complex microstructures, such as high-performance steels. Local-electrode atom-probe tomography is used to obtain atom-by-atom 3D reconstructions to characterize three versions of a copper, nickel, manganese, and aluminum bearing high-strength low-carbon steel, which achieve their high tensile yield strength, up to 1170 MPa (170 ksi), from the formation of nanometer-radius copper rich precipitates. The temporal evolution of these precipitates is followed at 500 °C, and it is found that manganese and nickel segregate at their interfaces with the segregation level increasing with aging time. The segregation of carbon, boron, phosphorous and sulfur at grain boundaries is detected and correlated with poorer impact fracture toughness at higher segregation levels.

Keywords: Precipitation strengthening; Interfacial segregation; Ferritic steels; Nanostructure; Temporal evolution

1. Introduction

High-strength low-carbon (HSLC) steels employing copper precipitation strengthening are important for the transportation, infrastructure, and defense industries because of their high strength, high ductility, and high impact toughness. These HSLC steels contain low carbon concentrations, making them less responsive to the formation of martensite during quenching. Since martensite and secondary carbide formation are not needed for strengthening in HSLC steels, elements such as Cr and Mo that are normally needed for hardenability can be omitted [1,2]. Benefits are the absence of toxic Cr^{6+} vapors during welding and reduced cost. The absence of martensite also prevents the formation of a brittle heat-affected-zone (HAZ) during welding. The ferritic microstructure means better cryogenic impact toughness and thus improved explosion resistance at low temperatures. Additionally, the alloying element Cu improves the atmospheric corrosion resistance and weatherability of the alloys [3].

The strength of Fe–Cu steels is derived from both solid-solution and precipitation strengthening. By adjusting the processing parameters the precipitation process can be controlled. This gives the ability to control the number density and mean radius of the precipitates, which determines directly the alloy's strength and impact toughness. Controlling the processing parameters can also reduce the cost in comparison to the quenching, tempering, and aging process of a steel containing martensite.

To control the number density and mean radius of precipitates and understand their temporal evolution, it is useful to observe them directly and measure these values in three dimensions with subnanometer spatial resolution. This ability is provided by the local-electrode atom-probe (LEAP™) tomograph [4–6]. The LEAP tomograph improves upon the conventional three-dimensional atom-probe (3DAP) tomograph by implementing a local extraction electrode (shown schematically in Fig. 1), faster solid-state high-voltage pulsers with pulse rates up to 2×10^5 Hz, variable voltage post-evaporation (secondary) accelerator and control electrodes, a 80–128 mm continuously adjustable flight

* Corresponding author. Address: Department of Materials Science and Engineering, Northwestern University, Evanston, IL 60208-3108, USA. Tel.: +1 847 491 3575; fax: +1 847 467 2269; e-mail: isheim@northwestern.edu

1359-6462/$ - see front matter © 2006 Acta Materialia Inc. Published by Elsevier Ltd. All rights reserved.
doi:10.1016/j.scriptamat.2006.02.040

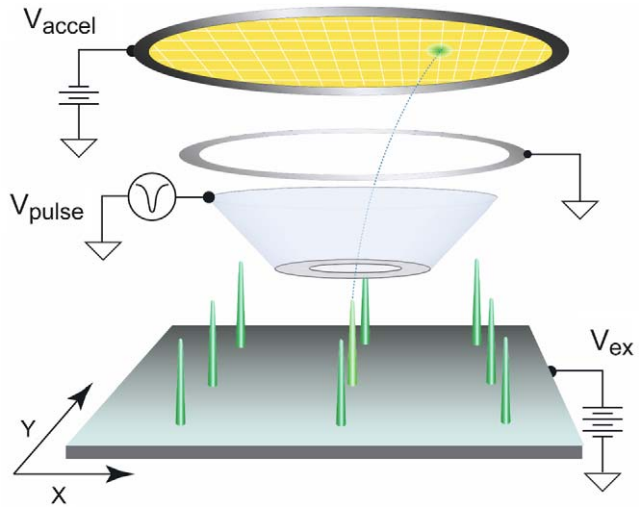

Figure 1. A schematic of a LEAP tomograph scanning a planar array of microtips using a high-voltage pulsed electric field. Also shown schematically is the variable voltage post-evaporation (secondary) accelerator, V_{accel}. Courtesy of Prof. Lincoln Lauhon, Northwestern University.

path, and a two-dimensional time-of-flight position sensitive delay-line detector with a collection rate that is $>1.2 \times 10^6$ ions min^{-1}. The LEAP tomograph achieves a mass resolution ($m/\Delta m$) of ~300–500 at full-width-half-maximum in a configuration with a significantly shorter flight path than the conventional 3DAP tomograph. The short flight path and the post-acceleration electrodes provide an adjustable field-of-view of up to 40°, thereby yielding larger analyzed volumes, $>10^6$ nm^3. The faster pulsing and data collection rates results in datasets as large as 1.25×10^8 ions for a single specimen. Furthermore, the use of a local electrode allows the analysis of a planar array of microtips in addition to the standard wire tip. Laser pulsing (femto- or picosecond) may also be used rather than voltage pulsing allowing the study of low electrical conductivity specimens.

Individual atoms are field-evaporated from the tip of a specimen (radius < 100 nm) using high-voltage pulses. The chemical identity of field-evaporated ions is identified by time-of-flight mass spectrometry. A delay-line position-sensitive detector determines the two-dimensional positions of the ions in the x–y plane, and the z-dimension is obtained from the sequence of field-evaporation events. As atoms are field-evaporated, features within the bulk of the specimens such as nanoscale precipitates, larger carbide precipitates, or grain boundaries are accessed. The position coordinates and chemical identity of each detected ion are then plotted in three-dimensional (3D) space, employing a computer and advanced software. A 3D reconstruction of the atoms is generated providing visualization of the features. In-depth quantitative results that include composition profiles, physical and chemical widths of interfaces, number density and mean radius of precipitates and carbides can also be obtained.

LEAP tomography was used to analyze two high-strength low-carbon iron-copper steels with different copper concentrations, Table 1. The lower-Cu concentration steel is denoted NUCu-150, where the number 150 stands for the yield strength of the steel in ksi (150 ksi = 1035 MPa). This comparatively high strength is achieved in combination with a Charpy V-notch impact toughness energy-adsorption value of 65 J (48 ft lb) at −40 °C (−40 °F). The higher-Cu concentration steel with a 1170 MPa (170 ksi) yield strength is denoted NUCu-170. The temporal evolution at 500 °C of the precipitates and their local composition are analyzed in the NUCu-150 (1st heat) steel. Other significant features such as cementite precipitation and grain boundary segregation of metalloid and impurity elements are also investigated. The precipitate radius and observed grain boundary segregation are correlated with mechanical properties.

2. Experimental methods

The alloys were vacuum induction melted and cast in 45.5 kg (100 lb) heats at Mittal-Ispat-Inland Inc. Research Center. The heats were hot-rolled to 12.5 mm (1/2 in.) thick plates and air-cooled. The plates were cut into rods $12.5 \times 12.5 \times 250$ mm and solution treated at 900 °C for 40 min, followed by a room temperature water quench. The rods were cut into $12.5 \times 12.5 \times 25$ mm blanks for a mechanical property study [7] and aged for different times at 500 °C.

Specimens were cut from the aged blanks and tips for atom-probe tomography (APT) were prepared by electropolishing. This involved using initially a solution of 10 vol.% perchloric acid in acetic acid at 8–20 V_{dc} at room temperature, and for final polishing a solution of 2 vol.% perchloric acid in butoxyethanol at 8–15 V_{dc} at room temperature was employed.

APT analyses were performed employing a LEAP 3000 tomograph manufactured by Imago Scientific Instruments Corporation, Madison, WI. The analyses were performed at a specimen temperature of 50 K, a pulse repetition frequency of 200 kHz, a pulse-voltage-to-dc-voltage ratio of 15–20%, and a residual pressure of $<1 \times 10^{-8}$ Pa. Visualization and quantitative evaluation of the 3D atom-by-atom datasets were performed with IVAS2.2 (Imago Scientific Instruments) and with ADAM 1.5, a custom software application developed at Northwestern University [8]. The compositional analysis of the copper-rich precipitates, their interfaces and adjacent matrix was performed with the proximity histogram method, or proxigram for short, implemented in ADAM 1.5 [9,10], which results in concentration profiles with respect to distance from a precipitate's surface. To perform the proxigram analysis, the copper-rich precipitates were discriminated by a 5 at.% Cu isoconcentration surface, obtained with a voxel size of 0.8–1.0 nm and a delocalization distance of 2.0 nm [11]. The confidence sigma parameter of ADAM 1.5 [9–11] was maintained at a value ⩽1 to achieve effective noise suppression. Neither the isoconcentration surface nor the proxigrams varied significantly within a certain range of these parameters, indicating a numerically stable evaluation procedure and thereby ensuring representative results.

Table 1. Compositions of high-strength low-carbon (HSLC) NUCu-steels studied

		C	Mn	P	S	Si	Cu	Ni	Al	Nb
NUCu-150 (1st heat)	wt.%	0.05	0.47	0.005	0.001	0.46	1.34	2.71	0.60	0.07
	at.%	0.23	0.47	0.009	0.002	0.91	1.17	2.55	1.23	0.04
NUCu-150 (2nd heat)	wt.%	0.04	0.48	0.014	0.004	0.48	1.37	2.86	0.69	0.07
	at.%	0.18	0.48	0.025	0.007	0.94	1.19	2.69	1.41	0.04
NuCu-170	wt.%	0.05	0.50	0.01	0.003	0.51	2.09	2.83	0.68	0.07
	at.%	0.23	0.50	0.018	0.005	1.00	1.82	2.67	1.39	0.04

The radius, R, of a precipitate containing n atoms in a reconstruction, was equated to the diameter of the volume equivalent sphere,

$$R = \left(\frac{3}{4\pi}\frac{n\Omega}{f}\right)^{\frac{1}{3}}, \quad (1)$$

where the atomic volume, Ω, is 1.178×10^{-2} nm^3 for bcc Fe, and the overall detection and reconstruction efficiency, f, was estimated to be 0.5. The value of n belonging to a precipitate was determined employing the envelope method [12], based on clusters containing more than 20 copper atoms separated not farther than a maximum separation distance of 0.5 nm and employing an envelope grid spacing of 0.15 nm.

3. Results and discussion

3.1. Temporal evolution of copper-rich precipitates in NUCu-150

Figure 2 displays 3D atom-by-atom LEAP tomography reconstructions of sample volumes from the NUCu-150 (1st heat) steel after aging at 500 °C for 3 h, 24 h, or 100 h. This span of aging times coincides with the period needed to achieve the maximum tensile strength of 1035 MPa (150 ksi) [2]. A comparison of the three reconstructions (Fig. 2(a)–(c)) permits following the temporal evolution of copper precipitates distributed homogeneously labeled "A". An increase of the diameter of copper-rich precipitates, with the Cu atoms shown in red, is evident with increasing aging time from (a) 3 h to (c) 100 h. Additionally, it is seen qualitatively that nickel (green dots) and manganese (maroon dots) atoms segregate at the Cu-rich precipitates/matrix interface. The segregation enhancement of Ni and Mn atoms evolves temporally, and after 100 h aging a distinct layer enriched in Ni and Mn can be seen enveloping the precipitates labeled "D" in Figure 2(c), while precipitates that are cut by the surface of the reconstructed volume labeled "A" have their copper-rich cores exposed. In addition to the small homogeneously distributed Cu-rich precipitates labeled "A", a cementite precipitate, "B", is discernible at the top of Figure 2(a) by its high carbon concentration, black dots. Compositional analysis of this precipitate resulted in a concentration of 66.7Fe–2.8Ni–0.9Cu–0.3Al–0.6Mn–0.1Si–28.4C (at.%), indicating the presence of Fe_3C-type cementite. In the vicinity of that cementite precipitate, larger Cu-rich precipitates have formed, labeled "C" in Figure 2(a). Next to these larger Cu-rich precipitates is a region enriched in Ni (green dots) and Al (yellow dots) atoms, which is distinct from the precipitates and different from the aforementioned segregation layer of Ni and Mn that evolves temporally and is surrounding the homogeneously distributed Cu-rich precipitates. It is clear that a full description on a nanometer scale of this complex three-dimensional nanostructure requires a detailed sophisticated analysis. We therefore next focus our attention on the segregation shell enveloping the homogeneously distributed Cu-rich precipitates.

Firstly, the homogeneously distributed Cu-rich precipitates are outlined by an isoconcentration surface drawn at the 5 at.% Cu level (Fig. 3(a)–(c)) encompassing all areas with a copper concentration greater than

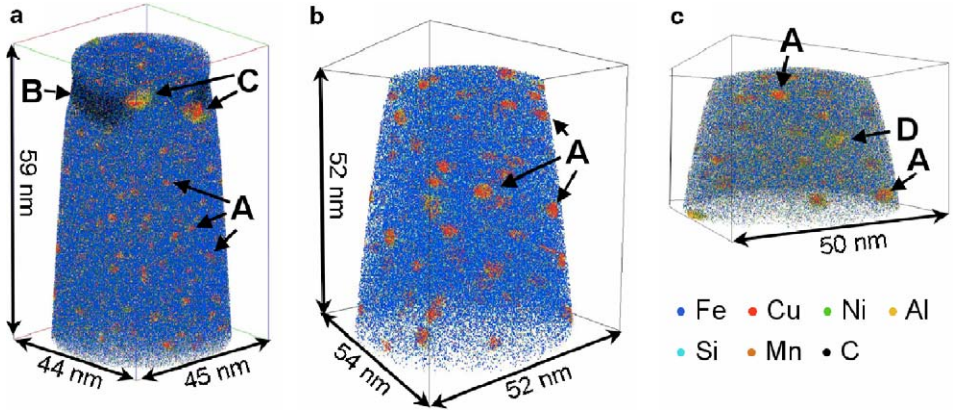

Figure 2. Three-dimensional atom-by-atom atom-probe tomographic reconstructions of specimen volumes in a NUCu-150 (1st heat) steel after aging at 500 °C for (a) 3 h; (b) 24 h; or (c) 100 h, illustrating the temporal evolution of the copper-rich precipitates used for precipitation strengthening of this HSLC steel. The reconstructed volumes contain (a) 3.0 million atoms; (b) 3.3 million atoms; and (c) 2.6 million atoms.

this value. This representation permits a direct view of all Cu-rich precipitates and their 3D distribution. Secondly, compositional analyses of the precipitates, their interfaces, and the surrounding matrix, are achieved by employing this isoconcentration surface as a fiducial surface for proximity concentration profiles with respect to distance from it [9–11]. The resulting composition profiles for the three aging times investigated are displayed in Figure 4(a)–(c), thereby allowing us to track the evolving chemical compositions of the precipitates, their interfaces, and surrounding matrix, for up to 100 h aging time. The Cu-rich precipitates are represented at the right-hand side of the diagrams (positive distances), with the origin at the location of the original isoconcentration surface.

While the maximum copper concentration in the precipitate's center (far right-hand side of the diagrams) remains constant at about 50% during aging up to 100 h, the matrix/precipitate interface becomes sharper and the nickel and manganese concentrations distinctively increase in the interfacial region near the origin of the diagrams (black arrows). This implies that the precipitates develop a spherical shell enriched in Ni and Mn with increasing aging time from 3 h to 100 h, which may contribute to the observed increase in tensile strength up to 100 h aging [2]. The Ni and Mn shell is also likely to reduce precipitate growth and coarsening, which makes this high-strength low-alloy steel less prone to softening as a result of overaging of the precipitates.

The precipitates' diameters are determined using the maximum-separation method as described above. The resulting particle size distributions (PSDs) are displayed in Figure 5 for aging at 500 °C for (a) 3 h; (b) 24 h; or (c) 100 h. After 3 h aging, 208 precipitates are found in the reconstructed volume and the precipitate number density, N_V, is 3.3×10^{24} m^{-3}. The average precipitate radius, $\langle R \rangle$, is 0.9 nm. The value of $\langle R \rangle$ increases to 1.5 nm after 24 h aging and N_V decreases to 1.2×10^{24} m^{-3}. After 100 h aging, $\langle R \rangle$ is 1.8 nm and N_V has decreased further to 6.1×10^{23} m^{-3}, with 42 precipitates detected in the reconstructed volume. At this precipitate radius, the maximum strength of 1035 MPa (150 ksi) is achieved [2]. The concomitant increase in $\langle R \rangle$ with decreasing N_V indicates that the precipitation process has completed the nucleation phase.

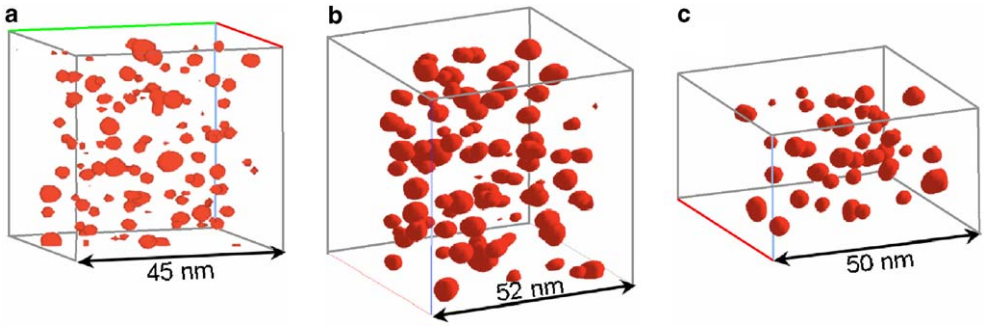

Figure 3. The copper-rich precipitates in the NUCu-150 (1st heat) steel are discernible more clearly after discriminating with an isoconcentration surface at a 5 at.% copper threshold level, after aging for (a) 3 h; (b) 24 h; or (c) 100 h.

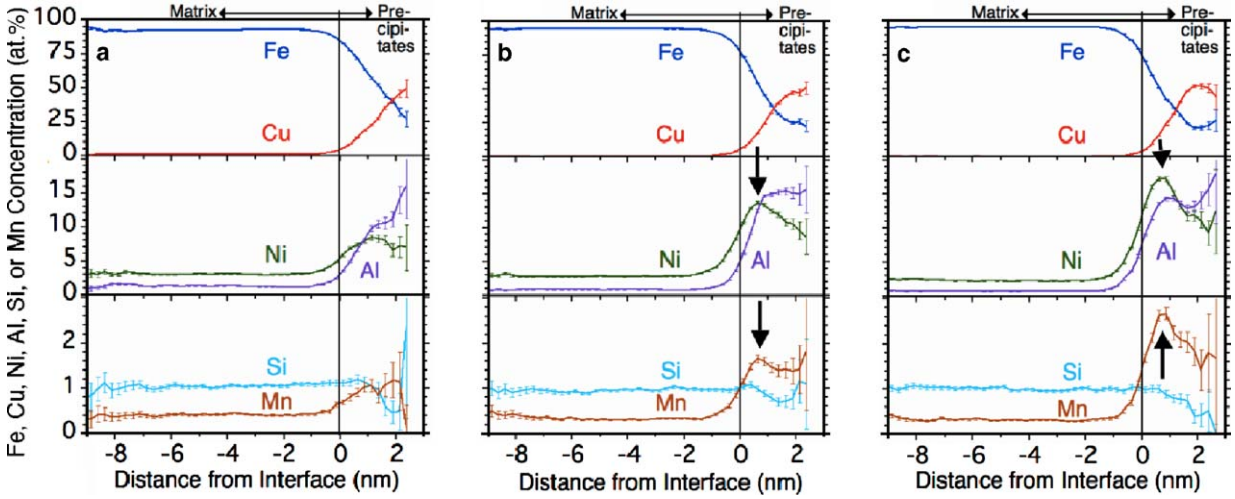

Figure 4. Proxigram concentration profiles for copper-rich precipitates in the NUCu-150 (1st heat) steel after aging at 500 °C for (a) 3 h; (b) 24 h; or (c) 100 h. The maximum copper concentration in the precipitates' centers remains at about 50% for aging times up to 100 h. The precipitates, however, develop a spherical shell enriched in Ni and Mn (black arrows). The error bars are the statistical uncertainty, $\sigma = \sqrt{c(1-c)/N}$ for a concentration c and N total atoms.

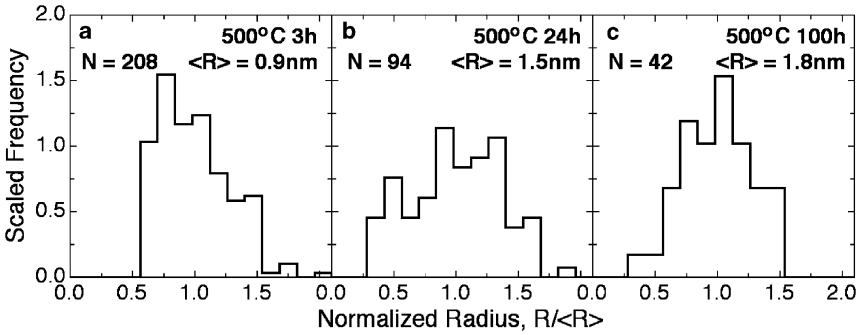

Figure 5. Particle size distributions of the homogeneously distributed copper-rich precipitates in NUCu-150 (1st heat) steel, after aging at 500 °C for (a) 3 h; (b) 24 h; or (c) 100 h.

3.2. Grain boundary segregation

Another important situation where a full three-dimensional atom-by-atom picture is very valuable is grain boundary segregation. The segregation of impurity and solute elements at the grain boundary greatly affects the mechanical properties. Segregants such as boron and carbon can increase the strength of the steel [13,14]. Other elements such as phosphorous, silicon, or manganese have been shown to embrittle steels [15]. The combined effect with multiple impurities at a grain boundary can also be studied using LEAP tomography. The APT technique, unlike Auger electron spectroscopy (AES), which has traditionally been used to study grain boundary segregation, can access segregation data without in situ fracture under an ultrahigh vacuum. Additionally, the APT technique does not disturb the atomic arrangement of the elements at a grain boundary and can provide direct spatial distribution data of atoms at the interface [16–18]. Figure 6 displays LEAP tomography atom-by-atom reconstructions of the segregation of carbon, boron, sulfur, and phosphorous at a grain boundary in NUCu-170 (Fig. 6(a)) and a grain boundary in NUCu-150 (1st heat) (Fig. 6(b)). The reconstructions demonstrate that these elements are more strongly segregated at a grain boundary in NUCu-170. The ratio of C:B:S:P is 10:3.8:2.8:3.2 for NUCu-170 but only 10:0.5:0.05:1.4 for NUCu-150 (1st heat). We have found that after aging at 500 °C for 4 h NUCu-170 has a reduced Charpy impact toughness of 16.3–20.3 J (12–15 ft lb) at room temperature. After aging at 500 °C for 2 h the second heat of NUCu-150 also exhibited a reduced toughness of 70.5 J (52 ft lb) at room temperature. Both compared poorly to NUCu-150 (1st heat) steel aged at 550 °C for 2 h, which has an impact toughness of 206 J (152 ft lb) at room temperature [7]. It is likely that grain boundary segregation of interstitial impurities as found in NUCu-170, plays a significant role in embrittling grain boundaries.

4. Conclusion

Atom-probe tomography was used to investigate HSLC steels, which achieve high tensile yield strengths of up to 1170 MPa (170 ksi) from nanometer-scale copper rich precipitates. Their temporal evolution was followed at 500 °C, and it was found that manganese and

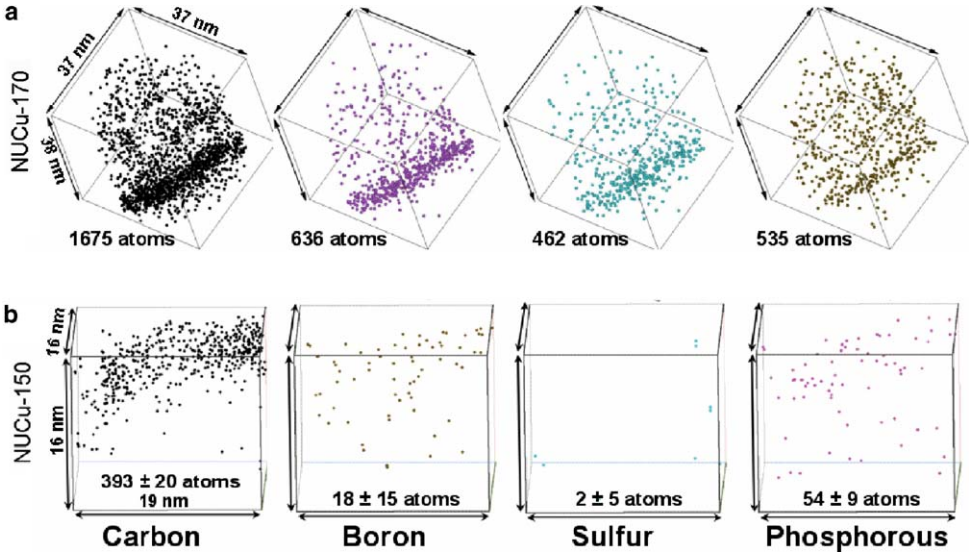

Figure 6. 3D APT atom-by-atom reconstructions of grain boundaries in (a) NUCu-170 steel and (b) NUCu-150 (1st heat) steel, displaying the distribution of carbon, boron, sulfur, and phosphorous atoms. Carbon is strongly segregated at grain boundaries in both steels. The alloy with the lower fracture toughness, NUCu-170, however, exhibits significantly higher levels of boron, sulfur, and phosphorous segregation.

nickel segregated at the interfaces of these precipitates with the segregation level increasing with aging time up to 100 h. The segregation of carbon, boron, phosphorous and sulfur at grain boundaries was detected and correlated with poorer impact fracture toughness at higher segregation levels.

Acknowledgements

This research is supported by the Office of Naval Research (N00014-03-1-0252); Dr. Julie Christodoulou, grant officer. Atom-probe tomographic analyses were performed at the Northwestern University Center for Atom-Probe Tomography (NUCAPT), and the LEAP tomograph was purchased with funding from the ONR-DURIP (N00014-0400798) and NSF-MRI (DMR-0420532) programs. Dr. Shrikant Bhat of Mittal-Ispat-Inland Steel Research Center is kindly thanked for providing the alloys used in this study. Semyon Vaynman, Northwestern University, is also kindly thanked for the provision of aged samples.

References

[1] M.E. Fine, R. Ramanathan, S. Vaynman, S.P. Bhat, in: Proceedings of the International Symposium on Low-carbon Steel of the 90's, Philadelphia, PA, 1993, p. 511.
[2] S. Vaynman, D. Isheim, M.E. Fine, D.N. Seidman, S.P. Bhat, in: Materials Science and Technology 2004 Conference Proceedings, New Orleans, AIST and TMS, vol. 1, 2004, pp. 525–530.
[3] S. Vaynman, M.E. Fine, in: R.I. Afsahani, R.L. Bodnar (Eds.), Proceedings of the International Symposium on Steel for Fabricated Structures, ASM International, Materials Park, OH, 1999, p. 59.
[4] S.S. Bajikar, D.J. Larson, T.F. Kelly, P.P. Camus, Ultramicroscopy 65 (1996) 119.
[5] T.F. Kelly, P.P. Camus, D.J. Larson, L.M. Holzman, S.S. Bajikar, Ultramicroscopy 62 (1996) 29.
[6] T.F. Kelly, D.J. Larson, Mater. Charact. 44 (2000) 59.
[7] S. Vaynman, unpublished research, 2005.
[8] O.C. Hellman, J. Vandenbroucke, J. Blatz du Rivage, D.N. Seidman, Mater. Sci. Eng. A 327 (2002) 29.
[9] O.C. Hellman, J.A. Vandenbroucke, J. Rüsing, D. Isheim, D.N. Seidman, Microsc. Microanal. 6 (2000) 437.
[10] O.C. Hellman, D.N. Seidman, Mater. Sci. Eng. A 327 (2002) 24.
[11] O.C. Hellman, J. Blatz du Rivage, D.N. Seidman, Ultramicroscopy 95 (2003) 199.
[12] M.K. Miller, Atom Probe Tomography, Kluwer Academic/Plenum Publishers, New York, NY, 2000, p. 158.
[13] C.M. Liu, N.K. Abiko, H. Kimura, Metall. Trans. A 23 (1992) 263.
[14] E. Yasyhara, K. Sakata, T. Kata, O. Hashimoto, ISIJ Int. 34 (1994) 99.
[15] M. Tetsuya, J. Shimomura, K. Seto, Mater. Trans. JIM 37 (1996) 323.
[16] B.W. Krakauer, D.N. Seidman, Phys. Rev. B 48 (1993) 6724.
[17] B.W. Krakauer, D.N. Seidman, Acta Mater. 46 (1998) 6145.
[18] D.N. Seidman, Annu. Rev. Mater. Res. 32 (2002) 235.